Geophysical Research Letters

RESEARCH LETTER
10.1029/2020GL089552

Hydrologic Properties of a Highly Permeable Firn Aquifer in the Wilkins Ice Shelf, Antarctica

Lynn Montgomery[1], Clément Miège[2], Julie Miller[3,4], Ted A. Scambos[3,4], Bruce Wallin[5], Olivia Miller[6], D. Kip Solomon[7], Richard Forster[8], and Lora Koenig[5]

[1]Department of Atmospheric and Oceanic Sciences, University of Colorado Boulder, Boulder, CO, USA, [2]Department of Geography, Rutgers University, Piscataway, NJ, USA, [3]Cooperative Institute for Research in Environmental Sciences, University of Colorado, Boulder, CO, USA, [4]Earth Science and Observation Center, University of Colorado, Boulder, CO, USA, [5]National Snow and Ice Data Center, Cooperative Institute for Research in Environmental Studies, Boulder, CO, USA, [6]United States Geological Survey, Utah Water Science Center, Salt Lake City, UT, USA, [7]Department of Geology and Geophysics, University of Utah, Salt Lake City, UT, USA, [8]Geography Department, University of Utah, Salt Lake City, UT, USA

Key Points:
- An extensive perennial firn aquifer within the Wilkins Ice Shelf is characterized for its hydrologic properties
- Field data and modeling show the aquifer has high permeability and is flowing into a nearby rift
- Past disintegration events on the Wilkins Ice Shelf with hydrofracture characteristics are likely a result of the aquifer's presence

Supporting Information:
- Supporting Information S1

Correspondence to:
L. Montgomery,
lynn.montgomery@colorado.edu

Citation:
Montgomery, L., Miège, C., Miller, J., Scambos, T. A., Wallin, B., Miller, O., et al. (2020). Hydrologic properties of a highly permeable firn aquifer in the Wilkins Ice Shelf, Antarctica. *Geophysical Research Letters*, *47*, e2020GL089552. https://doi.org/10.1029/2020GL089552

Received 29 JUN 2020
Accepted 19 OCT 2020
Accepted article online 29 OCT 2020

Abstract We present measurements of the density, hydraulic conductivity, and specific discharge of a widespread firn aquifer in Antarctica, within the Wilkins Ice Shelf. At the field site, the aquifer is 16.2 m thick, starting at 13.4 m from the snow surface and transitioning from water-saturated firn to ice at 29.6 m. Hydraulic conductivity derived from slug tests show a geometric mean value of $1.4 \pm 1.2 \times 10^{-4}$ m s^{-1}, equivalent to permeability of $2.6 \pm 2.2 \times 10^{-11}$ m^2. A borehole dilution test indicates an average specific discharge value of $1.9 \pm 2.8 \times 10^{-6}$ m s^{-1}. Ground-penetrating radar profiles and a groundwater flow model show the aquifer is draining laterally into a large nearby rift. Our findings indicate that the firn aquifer in the vicinity of the field site is likely not in a steady state and its presence likely contributed to past ice shelf instability.

Plain Language Summary Firn aquifers occur in areas of high melt and snow accumulation when meltwater percolates into firn (compacted snow older than 1 year) pore space and is stored throughout the winter without refreezing. In December 2018, a field team traveled to the Wilkins Ice Shelf on the Antarctic Peninsula and drilled into an aquifer. We used a combination of hydrology and ground-penetrating radar measurements to show that water is flowing laterally through porous buried snow and draining into a nearby rift. Firn aquifers are important since they allow meltwater to be stored at depth, possibly running off into cracks, crevasses, or rifts and increasing fracture depth, thereby leading to ice shelf destabilization.

1. Introduction

Ice shelves, extensions of ice sheets and glaciers that have thinned sufficiently to become afloat on the ocean, are prevalent around the Antarctic Ice Sheet (AIS) and play a role in restraining ice-sheet discharge into the ocean (Siegert et al., 2019). More than 80% of Antarctica's ice discharge is released through ice shelf outflow and basal melting, making them an integral control of the mass balance of the AIS (Pritchard et al., 2012; Rignot et al., 2013). Observations show that there are extensive surface hydrologic systems and meltwater storage on ice shelves in Antarctica (Bell et al., 2017; Kingslake et al., 2017; Lenaerts et al., 2017; Phillips, 1998) that can potentially accelerate their disintegration (Banwell et al., 2013; Scambos, 2004; Scambos et al., 2000). However, the meltwater volume, residence time, storage characteristics, and lateral/vertical movement remain not well understood despite being critical to estimate impacts on mass balance, ice dynamics, and sea-level changes (e.g., Bell et al., 2018; Lenaerts et al., 2019; Smith et al., 2020).

Firn aquifers, well documented in mountain glaciers (e.g., Fountain & Walder, 1998) and more recently discovered in Greenland and Svalbard (Christianson et al., 2015; Forster et al., 2014), form when meltwater produced at the surface percolates into the firn and fills the available pore space above the firn-ice transition without refreezing during winter. Firn aquifers are located where there is sufficient pore space volume in the firn column for meltwater to be stored and high accumulation, which provides insulation that permits the saturated subsurface layer to remain at 0°C (Forster et al., 2014; Kuipers Munneke et al., 2014). In Greenland, these conditions occur in the southeast, south, and northwest sectors where accumulation

rates are ~1–5 meters water equivalent (m w.e.) per year and melt rates are >650 mm WEyr^{-1} (Bell et al., 2018; Montgomery et al., 2020; Noël et al., 2018). For the AIS, areas with similar surface melt and snow accumulation signatures are rare, though recent modeling studies show widespread perennial firn aquifers on the Wilkins Ice Shelf (WIS) and elsewhere on the Antarctic Peninsula (van Wessem et al., 2016, 2020). These aquifers can contribute to sea-level rise if connected to the ocean by slowly draining into crevasses (Koenig et al., 2014) and are especially important to understand on ice shelves where meltwater storage is likely a precursor to hydrofracture and ice shelf break-ups (Bell et al., 2018; Scambos et al., 2000).

In December 2018, we conducted fieldwork on the WIS using a combination of borehole drilling, hydrological tests, and ground-penetrating radar (GPR) profiles. We used hydrological and geophysical measurements combined with a groundwater flow model to quantify lateral water flow and assess the hydrologic balance of the aquifer. Further, these results can be used in future studies to examine the impact of firn aquifers on ice shelf stability.

2. Study Site

Our field site is located on the southwestern portion of the WIS on the Antarctic Peninsula (Figure 1a). Measurements were taken ~50 km from the edge of the ice shelf (−70.80S, −71.71W) from 3–12 December 2018. Average (2010–2017) annual accumulation and melt rates simulated from two regional climate models (MAR and RACMO2) at the field site are 590–800 and 250–425 mm WEyr^{-1} (Figure 1c and Table S1 in the supporting information) (Agosta et al., 2019; Datta et al., 2018, 2019; Noël et al., 2018). A 17 km long rift in the ice shelf was observed ~5 km from our field site (Figure 1b).

Analysis of NASA Operation IceBridge 2014 radio-echo-sounding profiles collected over the WIS using the Multichannel Coherent Radar Depth Sounder (MCoRDS; CReSIS, 2020) indicated a bright reflector in the upper firn similar to high-amplitude reflections associated with firn aquifers for the Greenland Ice Sheet (Forster et al., 2014; Miège et al., 2016). Based on the separation of the snow surface reflection and the bright subsurface return, we anticipated the top of the firn aquifer to be ~13 m below the surface (Figure S1; Studinger, 2014). MCoRDS processing steps to retrieve aquifer extent and depth to water are discussed in detail in Miège et al. (2016) and Brangers et al. (2020).

3. Methods

3.1. Borehole Drilling and Firn/Ice Cores

We used a custom-built lightweight electrothermal drill to drill three boreholes located ~1 m apart, reaching depths of 14, 20, and 35 m to estimate density, stratigraphy, and use for other hydrological tests. Drill specifications are in the supplemental material of Miller et al. (2018). To determine gravimetric density, core sections (average diameter of 55 mm) were weighed and measured immediately after collection. The average uncertainties of these density measurements ranged from 9–11%, similar to previous studies (Text S5; Conger & McClung, 2009; Fornasini, 2008). We anticipate some meltwater to have drained during extraction and prior to weighing but cannot quantify the added uncertainty to the density measurements. The stratigraphy was recorded, and two main facies were identified: firn and ice lenses (Figures 2a and S2). No section of the retrieved core had temperatures substantially different from 0°C within the aquifer (accuracy ~ ±0.5°C).

3.2. Hydraulic Conductivity Estimate

Slug tests are used to measure the hydraulic conductivity in the saturated zone of an aquifer. Before the slug tests, we placed a pressure transducer (HOBO Onset© U20-001-02) with an operational range between 0 and 400 kPa and a maximum error of 3 cm of water at the bottom of the borehole, which allowed us to record the water-level changes (Figure S3a). To perform a slug test, we measured the time it took to displace a small volume of water by inserting/removing a solid cylinder (1,187.7 cm^3) into the water-filled part of the borehole and measuring the response time for the water level to return to its initial level (Figure S3c). We use present measurements from six slug tests (with the least noise) from 9–11 December 2018 in the 20 m borehole.

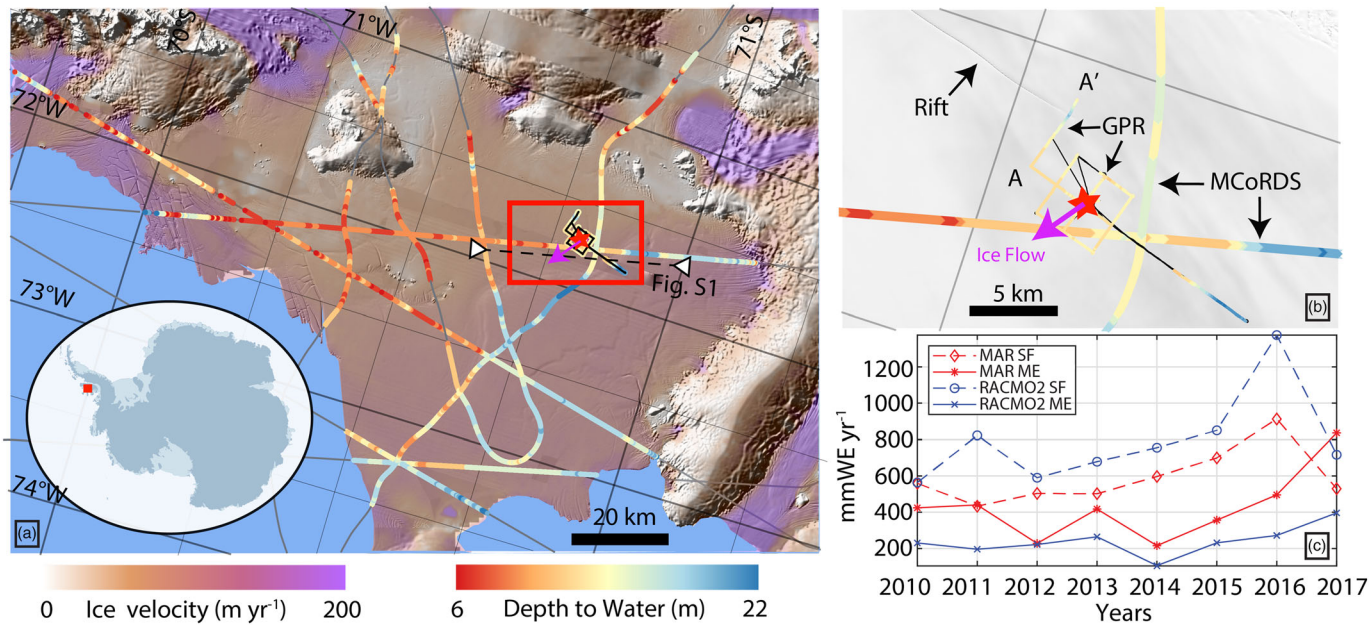

Figure 1. (a) Field site location (black star in the red square) on the Wilkins Ice Shelf. The depths to the water table (blue-orange color bar) are derived from the MCoRDS radar system (CReSIS, 2020), a part of NASA's Operation IceBridge flight on 16 November 2014 (Figure S1). The background is a hillshaded DEM (REMA; Howat et al., 2019). (b) Close-up of our field site (black star; the image is from Landsat 8, 24 February 2020) with Operation IceBridge (OIB) aquifer detections (large circles) along with water-table estimates from our GPR surveys (small circles) around camp and across an adjacent ice shelf rift. Black lines show areas with GPS data only. The magenta arrow represents the direction of surface velocity based on an 8-day continuous GPS record. (c) Time-series of annual snowfall (SF) and melt (ME) for 2010–2017 as simulated by both RACMO2 and MAR at the field site.

3.3. Borehole Dilution Test

We used a saline dilution method in the 35 m borehole to estimate discharge through the aquifer and locate the base of the flow zone. This method is established for traditional groundwater studies (Pitrak et al., 2007) and was recently adapted for estimating water discharge within firn aquifers in the Greenland Ice Sheet (Miller et al., 2018). The method consists of injecting a saline solution of a known conductivity into the borehole and monitoring the conductivity variation over time throughout the borehole to estimate horizontal flow through permeable firn. A description of the method is in the supporting information (Text S1 and Figure S4). After injecting and homogenizing the salt solution in the borehole, vertical conductivity profiles were recorded with a vertical spacing of 30 cm in the water-filled part of the borehole: every 30 min for the first four profiles, followed by two profiles taken an hour apart, then two more profiles taken 2 hours apart (Figure 2b). One additional profile was taken the following morning. The total duration of the experiment was ~17 hours. This borehole dilution test also allows us to estimate specific discharge and linear velocity with depth (Figures 2b and 2c).

3.4. Geophysical Surveys and Water-Table Elevation Estimates

We used GPR to survey the top ~50 m of the firn/ice column and identify the water-table depth around the drilling site and rift. We also surveyed ~35 km of surface topography using a GPS receiver. Limited postprocessing was required because the water table was easily identified as a high-reflective high-amplitude signal. Postprocessing included shifting the traces vertically to align the surface with the first break position of the signal, geolocation, adjustment for surface elevation, and removing the mean trace for the profiles from each trace within the profiles to enhance layering details. We converted from two-way-travel time to depth using mean density from the cores above the water table and a relationship linking permittivity and density (Kovacs et al., 1995). Details of the GPR method are in the supporting information (Text S2).

We also conducted an 8-day continuous GPS survey (1-s epochs) at the drill site (3–11 December 2018) to determine the short-term ice flow vector and tidal range (Figure S5). Ice flow speed was 92.8 m d^{-1} with a

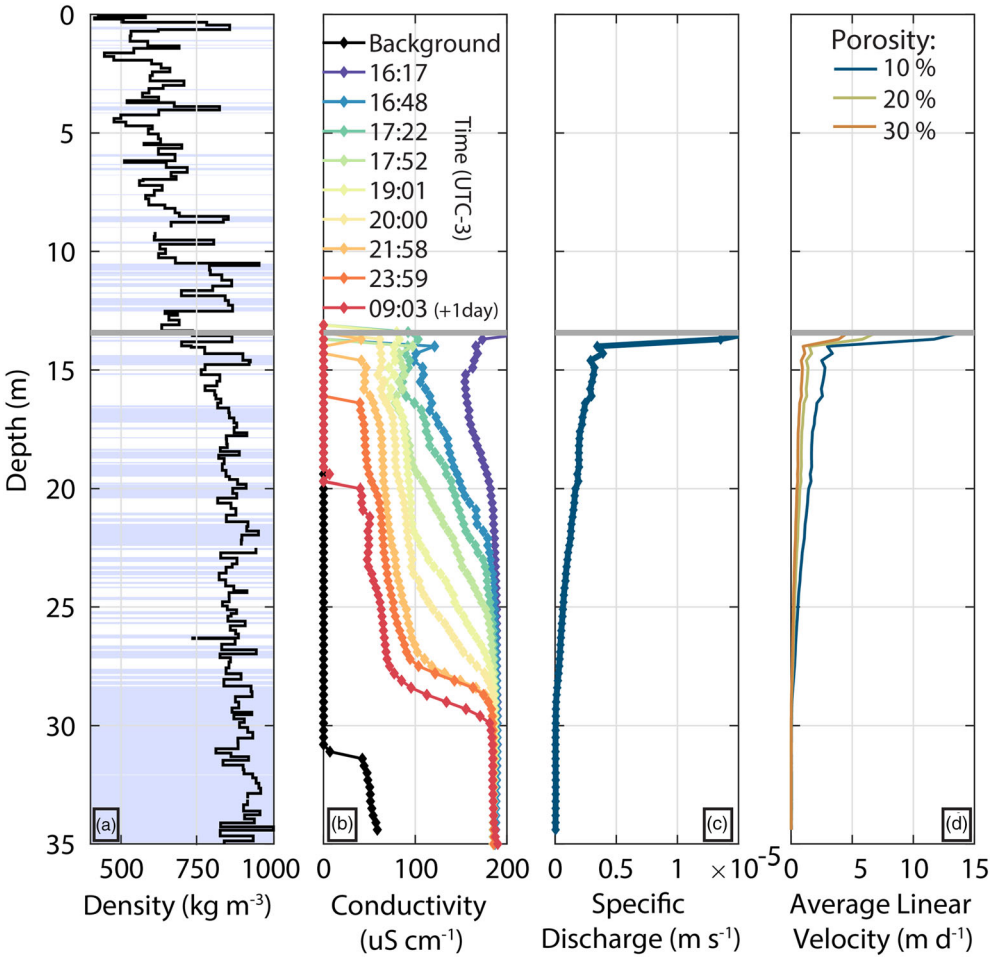

Figure 2. Firn characteristics and dilution test results. (a) Core properties (density and stratigraphy) through the firn aquifer. Blue bands indicate ice layers, white indicates porous firn, and the gray line corresponds to the water table. The base of the aquifer is indicated by the lowest ice-dominated ~29–35 m. (b) Salt dilution time series. The black line shows the background characteristics of the aquifer, including a nonzero salinity within the basal ice layer. Color lines and their start times (UTC-3) represent successive conductivity vertical profiles after salt added to the borehole (10–11 December 2018). (c) Resulting specific discharge estimated from the dilution rate. (d) Average linear velocity interpreted from the dilution rate assuming different porosities.

near-zero diurnal variation. The daily range of vertical ice motion, roughly equal to tidal motion, was 0.8 to 1.3 m.

Both GPS-receiver signals were processed using the precise point positioning (PPP) web-based processor hosted by the Canadian Spatial Reference Service (CSRS; https://webapp.geod.nrcan.gc.ca/geod/tools-outils/ppp.php).

3.5. Flow-Rate Modeling

We use SEEP2D (Jones, 1999), a 2-D finite element flow model within the Groundwater Modeling System package, to simulate water flow within the aquifer, based on the results of the slug tests, GPR, and firn core measurements to determine if the aquifer is in steady state and constrain recharge estimates. SEEP2D solves the steady-state (i.e., all recharge that reaches the aquifer is discharged into the rift) groundwater flow equation (Cherry & Freeze, 1979) that is based on mass balance and utilizes Darcy's Law calculated as

$$\frac{Q}{A} = -K\frac{\partial H}{dx}$$

where Q is groundwater flow ($m^3\ s^{-1}$), A is cross-sectional area (m^2), K is the hydraulic conductivity

($m\ s^{-1}$), and $\partial H/\partial x$ is the slope of the water table. Details of the SEEP2D model setup and assumptions are in the supporting information (Text S3).

We ran SEEP2D simulations with the following recharge scenarios:

1. High Recharge (*MAR and RACMO2*): 100% of surface meltwater (425 mmWE yr^{-1}), MAR; and (250 mmWE yr^{-1}), RACMO2 recharges the aquifer, with no refrozen melt in the firn.
2. Medium Recharge (*RACMO2*): 50% of surface meltwater (125 mmWE yr^{-1}) recharges the aquifer, 50% of meltwater is refrozen.
3. Low Recharge (*RACMO2*): 25% of surface meltwater (62.5 mmWE yr^{-1}) recharges the aquifer, 75% of meltwater is refrozen.
4. Low Recharge (*MAR*): 10% of surface meltwater (42.5 mmWE yr^{-1}) recharges the aquifer, 90% of meltwater is refrozen.

Recharge scenarios were chosen to represent a wide range of possible climatic conditions on the ice shelf. We compare these steady-state output conditions (water table slope and aquifer thickness) to our observations to determine if these scenarios are plausible. One test of plausibility is to compare the amount of refrozen meltwater in the simulation to the column fraction of ice lenses in the firn core density profile.

4. Results

4.1. Firn Core Characteristics

The deepest firn core was collected at 35 m, below the estimated firn-ice transition of ~29.6 m (when the specific discharge reaches 0; Figure 2c). The average firn density above the aquifer was 650 kg m^{-3} and within the aquifer was 850 kg m^{-3} (Figure 2a). Two shallower firn cores were collected 1 m away from the deepest firn core and show small-scale spatial variability in density above the aquifer with average densities of 627 and 669 kg m^{-3} (Figure S2), which agree within 9–11% uncertainty. The three firn cores also show variability in ice lenses, with an ice fraction above the aquifer varying from 17.9% to 20.3% and an average of 18.1%. We measured the depth to water table, which ranged from 13.39–13.46 m, averaging 13.43 m, proving a homogeneous water table depth at the site. We compare this measured depth with the GPR depth converted from two-way-travel time and find a good agreement (±20 cm).

4.2. Hydraulic Conductivity

We derived values of hydraulic conductivity from slug tests ranging from 1.0×10^{-4} to 1.7×10^{-4} with a geometric mean of $1.4 \pm 1.2 \times 10^{-4}$ m s^{-1}. These correspond to permeabilities ranging from 1.8×10^{-11} to 3.1×10^{-11} m^2 and averaging $2.6 \pm 2.2 \times 10^{-11}$ m^2. Water level change values ranged from 10 to 15 cm (Figure S3). The slug tests indicate a highly permeable aquifer (similar to unconsolidated sand) with similar hydraulic conductivity values to that of the firn aquifer found in Southeast Greenland (Miller et al., 2017).

4.3. Borehole Dilution Test

A time series of conductivity profiles from the 35 m borehole after the saline solution was injected is shown in Figure 2b. We note that this conductivity represents a vertical profile of salinity and not hydraulic conductivity. The background conductivity is below detection until ~30 m, where it increased to 75 μS cm^{-1}. After the conductivity reached 200 μS cm^{-1} in the water-filled borehole (Text S1), we observed a gradual decrease in the conductivity above 20 m until background levels were reached. Below 20 m, the conductivity did not reach background levels during our experiment time. The decrease in conductivity over time in the profiles indicates lateral water flow, which dominates the freshening process in the borehole. We consider diffusion rates to be negligible in this process as they are ~30 times smaller than the inferred advection of water. The decrease in dilution rate with depth (and therefore lateral flow) is primarily due to decreasing porosity. The profile reaches a pore close-off at ~30 m, eliminating any dilution or lateral flow (Figure 2a).

The vertical specific discharge (Text S4) profile derived from the salt dilution indicates where and the rate at which water flows laterally in the borehole profile into connected pores in the surrounding aquifer (Figure 2c). The bottom depth of the specific discharge profile where flow ceases (29.6 m) agrees with the bottom depth of the aquifer we found through coring (~29 m). The average specific discharge is 1.9×10^{-6} m s^{-1} with a maximum value of 1.6×10^{-5} m s^{-1} at the top of the aquifer due to high porosity

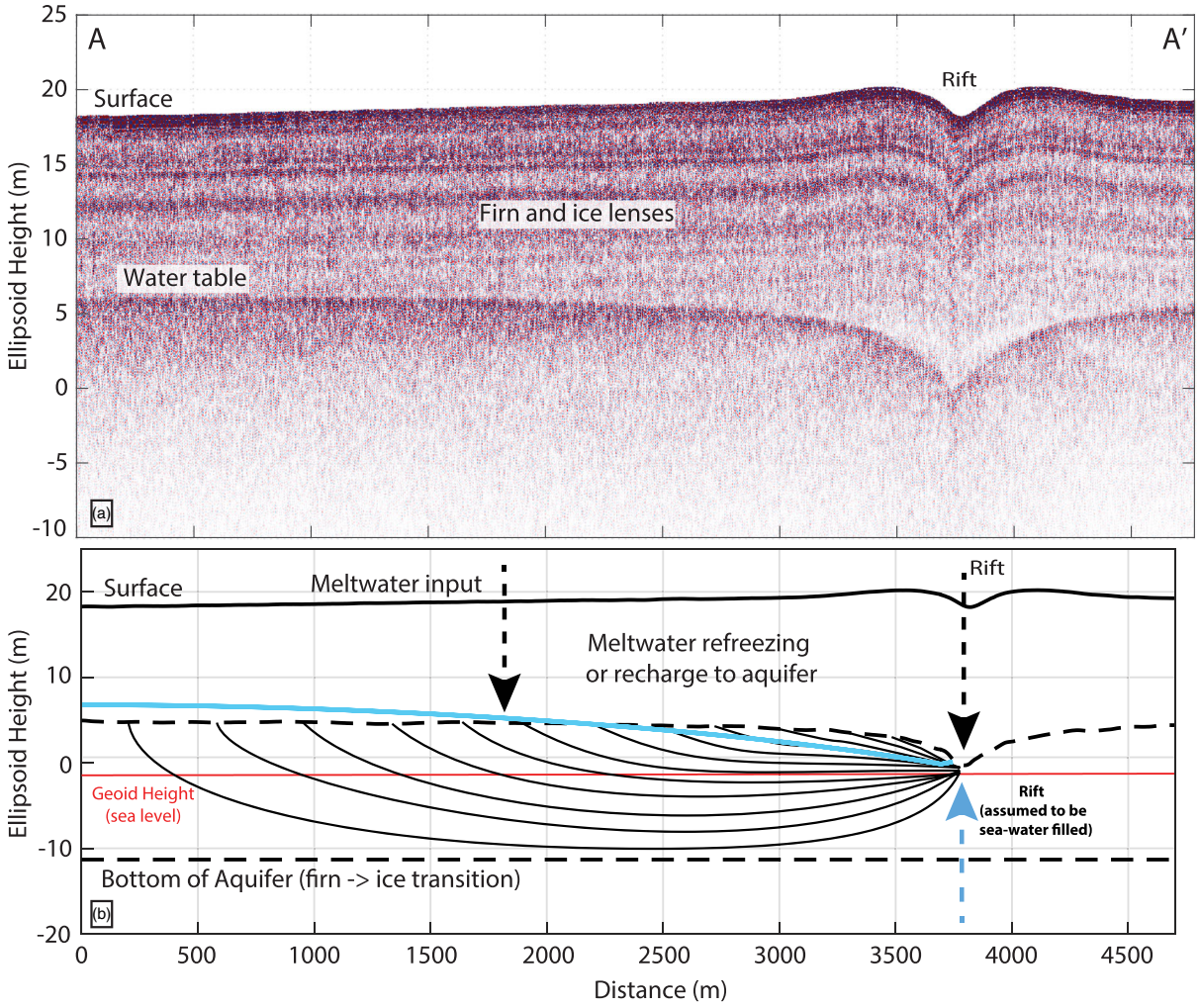

Figure 3. GPR profile across the rift and analysis of water flow and drainage of the firn aquifer layer. (a) GPR profile taken across a 5 km transect of the WIS. The high-reflective high-amplitude internal reflector ranging between 12 and 17 m below the surface is inferred to be the top of the firn aquifer. This begins to slope downward into an ice shelf rift 3.8 km from the start of the profile. Layering above the aquifer reflector represents ice layers within porous firn. (b) Schematic showing structure of aquifer and processes occurring in the snowpack. Solid black lines within the aquifer show flowlines resulting from meltwater input. The teal line shows the water table from the RACMO2 Low Recharge scenario.

values, which results in a standard deviation (σ) of 2.8×10^{-6} m s^{-1}. However, if we omit the maximum outliers, specific discharge σ decreases to 1.1×10^{-6} m s^{-1}.

We also calculated the average linear velocity profiles using uniform porosities ranging from 0.1 to 0.3 (Figure 2d and Text S4; Koenig et al., 2014). The density measurements in the region just above the aquifer suggest that the porosity is near the high end of this range at the top of the aquifer (Figure 2a). The average linear water velocity ranged from 0.6–1.7 m d^{-1} depending on the porosity. Our maximum linear velocity value was 14.1 m d^{-1} assuming a porosity of 0.1. The calculated values of linear water velocity are substantially larger than the measured ice motion (0.25 m d^{-1}); therefore, the water flow is faster than the surrounding ice flow.

4.4. GPR Survey of the Rift

The combined GPR-GPS radar profile from the field site across the southern terminus of the ice shelf rift (~5 km) indicates the surface of the ice shelf is initially ~17 m above the WGS84 ellipsoid height and rises to ~20 m within a few hundred meters of the rift location (3.8 km along the profile) before tipping downward toward the rift (Figures 1b and 3a). This profile shape is typical of rifts in ice shelves (e.g., Fricker et al., 2005). A survey of Landsat imagery (www.earthexplorer.usgs.gov) showed that the rift appeared in late 2009,

shortly after a series of major disintegration events on the WIS (Humbert et al., 2010). Rifts (breaks through the entire ice shelf) generally occur when tensile stresses exceed the tensile strength of the ice plate (Braun et al., 2009; Scambos et al., 2009). The rift was filled with snow at the southern end.

The profile reveals firn and ice lenses parallel to the ice shelf surface (Figure 3a) and a continuous strong reflector at the same depth (±1 m) as the aquifer's upper surface at the core site. No layering is observed below the bright layer, consistent with the radar attenuation expected for an aquifer layer. As the profile approaches the rift, it shows the inferred aquifer surface deepening and crossing the firn ice layering. The inferred aquifer surface intersects the rift at an ellipsoidal height of about 0 m, close to the local sea level (Figure 3b). Decreasing aquifer height and consequently decreasing hydraulic head toward the rift strongly implies the lateral movement of water toward the rift and drainage through its sidewalls.

4.5. Groundwater Flow Modeling

To quantitatively evaluate that water is flowing into the rift (thereby removing some of the annual recharge to the aquifer) and constrain the parameters in which the aquifer system would be in steady state, we use the SEEP2D groundwater flow model. Table S2 shows the results of the SEEP2D modeling.

First, we present two extreme scenarios of a steady-state aquifer where all surface melt, ranging from 250 to 425 mmWE yr^{-1} depending on the RCM used, recharges the aquifer. The $\partial H/\partial x$ (slope) and A (thickness) parameters required for the high recharge scenario contribution would be physically impossible compared to our observations because the water table of the aquifer is not 26–46 m (Table S2) above the firn-ice transition (i.e., we see no ponding). Further, the presence of refrozen melt layers in the upper firn suggests that the aquifer is not being recharged by all surface meltwater.

We also examine a recharge scenario where 125 mm WEyr^{-1} (50%) of surface melt recharges the aquifer, using RACMO2 melt input. The other half of the melt input refreezes or densifies the snowpack, which could explain the ice layers in the stratigraphy above the aquifer. However, steady state is only reached if the hydraulic conductivity is twice the observed value, the $\partial H/\partial x$ has a 13 m gradient over 3,800 m distance, or if the aquifer is twice as thick. Major dynamical or structural changes would have to occur in a short distance for this scenario to be plausible.

Our final scenarios present low meltwater recharge values ranging from 42.5 to 62.5 mmWE yr^{-1}, consequently leading to 75–90% of the melt input refreezing in the firn above. With this small amount of melt recharging to the aquifer, our model output matches closely with field measurements (Figure 3b). However, the ice fraction above the aquifer measured at our study site is too small to represent this amount of refrozen meltwater per year (i.e., no thick ice layers).

5. Discussion and Conclusions

We provide the first measurements of hydraulic conductivity, density, and specific discharge of a firn aquifer on an ice shelf in Antarctica. We also show that the water in this firn aquifer at this field site likely is discharging into a nearby rift. These measurements were performed at only one location but allow us some insight into the meltwater storage in the WIS. Further field experiments spatially distributed (i.e., seismic refraction, magnetic resonance, hydrological tests, and firn stratigraphy and density profiles) would be necessary to fully quantify the overall structure and age of the aquifer, various drainage divides, and the magnitude of the total discharge into the rift.

The average hydraulic conductivity value for the WIS aquifer (from slug tests, $1.4 \times 10^{-4} \pm 1.2$ m s^{-1}) is of the same magnitude but potentially below what was measured in Greenland ($2.7 \times 10^{-4} \pm 1.6$ m s^{-1}). In turn, the specific discharge from dilution tests (1.9×10^{-6} ms^{-1}, $\sigma = 2.8 \times 10^{-6}$ m s^{-1}) is also less than the value (4.3×10^{-6} m s^{-1}, $\sigma = 2.5 \times 10^{-6}$ m s^{-1}) from Greenland. This results from the smaller surface slope relative to the Helheim study area (~0° vs. 0.8°; Forster et al., 2014) and also suggests that there is less recharge on the ice shelf. The lower recharge rates can be explained by the lower melt rates compared to the Helheim Glacier region. In fact, both the modeled WIS accumulation and melt rates are less than half of the values in the southeastern Greenland region (590–800 and 250–425 [Figure 1c] vs. 1,400–1,650 and 730 mm WEyr^{-1}; Miège et al., 2016). Miller et al. (2017, 2018) found that the Greenland firn aquifer was highly permeable and had evidence of direct meltwater flow. This meltwater likely flowed into nearby crevasses and

possibly down to the bed of the ice sheet into the ocean (Poinar et al., 2017). Similarly, we find that the WIS firn aquifer is highly permeable and is likely discharging into the nearby rift.

Our hydrological modeling results indicate that while plausible, it is unlikely that the WIS aquifer is in steady state with all meltwater discharged to a nearby rift. The high recharge scenario was deemed implausible because hydraulic gradients rose above the ice shelf surface. The medium recharge scenario provided a more plausible ratio of recharge to refreeze and approximately accounts for the ice fraction of 18% observed in the core above the aquifer. To achieve steady state, this scenario either requires a water table slope or hydraulic conductivity that is two times greater than our observed values. Since we had to extrapolate our single hydraulic conductivity measurement value throughout the entire system, the variability of K in the system could explain the discrepancy. It is also possible that refreezing at the base of the aquifer accounts for some of the unexplained water mass. The low recharge scenarios both match the observed water table (Figure 3b), though this implies that 75–90% of the meltwater input densifies or is refrozen in the firn column above the aquifer, which does not agree with the observed ice fraction above the aquifer (Figure 2a). However, meltwater is required to bring the firn to an isothermal state above the aquifer to allow recharge after the winter season, which varies annually based on seasonal snow thickness and temperature, and could explain some excess meltwater (Miller et al., 2020).

We assume that our study site on the WIS firn aquifer is slowly draining into a large rift that was formed in 2009. Earlier observations using airborne radar show a highly reflective high-amplitude internal reflector near the surface (1966 and 1975 surveys; Operation IceBridge [OIB] surveys in 2014 shown in Figure 1) absent of any observed widespread surface flooding, even in the highest-melt years (Braun et al., 2009; Scambos et al., 2000; Vaughan et al., 1993). The presence and thickness of an aquifer are controlled primarily by the summer meltwater flux and the annual net snowfall and rainfall and to a lesser extent by freezing at the base of the aquifer column (Montgomery et al., 2017). Without surface flooding or complete refreeze seen from satellite imagery for several decades (Barrand et al., 2013; Braun et al., 2009; Scambos et al., 2000; Vaughan et al., 1993), the WIS has apparently maintained a near-balanced system with respect to water table height and therefore snowfall and recharge conditions. However, the specific dynamics of the past WIS aquifer are unknown, including if it was in steady state and has always had cracks in the ice shelf with which to evacuate water.

Firn aquifers offer sufficient water storage capacity to contribute to ice shelf disintegration events, as evidenced by the partial break-ups of the northern and northwestern WIS in 1993, 1998, and 2008–2009, where the bright reflector from airborne radar was present (Braun et al., 2009; Humbert & Braun, 2008; Scambos et al., 2000). Our study supports this conclusion, identifying the WIS aquifer as having high permeability and the drainage of the aquifer into the adjacent rift. However, the stability of an aquifer-bearing ice shelf will be dependent on the volume of the aquifer and relationship to the lateral flow of water within the aquifer. Discharge from firn aquifers has been modeled to be able to cause hydrofracturing to the bed of ice sheets with enough inflow of meltwater (Poinar et al., 2017). If a series of low melt years or high snowfall years decreased the relative height of the top of the aquifer column, the potential for hydrofracture is greatly reduced. The year-round availability of water at depth allows for enhanced fracturing whenever stresses change to favor tensile extensions or loss of compression, even in the winter (Scambos et al., 2009). With complete saturation of the vertical firn column, the hydrostatic head for hydrofracture is at a maximum value and has the potential to cause destabilization of ice shelves and iceberg calving through hydrofracturing (Bell et al., 2017; Pollard et al., 2015; Scambos et al., 2003, 2009). Continued and improved monitoring of firn aquifers would lead to a better understanding of the role these aquifers play in ice-shelf disintegration.

Data Availability Statement

All data used in this manuscript can be found at https://www.usap-dc.org/view/dataset/601390.

References

Agosta, C., Amory, C., Kittel, C., Orsi, A., Favier, V., Gallée, H., et al. (2019). Estimation of the Antarctic surface mass balance using the regional climate model MAR (1979–2015) and identification of dominant processes. *The Cryosphere*, *13*(1), 281–296. https://doi.org/10.5194/tc-13-281-2019

Banwell, A. F., MacAyeal, D. R., & Sergienko, O. V. (2013). Breakup of the Larsen B Ice Shelf triggered by chain reaction drainage of supraglacial lakes. *Geophysical Research Letters*, *40*, 5872–5876. https://doi.org/10.1002/2013GL057694

Acknowledgments

This work was supported by a National Science Foundation (NSF) Grant ANT-1745116. C.M. was partly supported by NSF Grant ARC-1604058. We appreciate the constructive and thorough reviews by Elizabeth Case, Jonny Kingslake, Annie Putman, and Baptiste Vandecrux, which greatly improved this manuscript. We thank our Editor Mathieu Morlighem for handling our manuscript. We acknowledge and express our gratitude to the British Antarctic Survey for outstanding field and logistics support, including our exceptional field guide, Tom Lawfield. We also thank Tri Datta, Christoph Kittel, and Brice Noël for providing model output from MAR and RACMO2. We thank Michelle Koutnik for lending us her conductivity probe. We acknowledge UNAVCO for lending us two GPS receivers. We acknowledge the use of data and/or data products from CReSIS generated with support from the University of Kansas, NASA Operation IceBridge grant NNX16AH54G, NSF grants ACI-1443054, OPP-1739003, and IIS-1838230, Lilly Endowment Incorporated, and Indiana METACyt Initiative. *REMA DEM* (Figure 1) is provided by the Byrd Polar and Climate Research Center and the Polar Geospatial Center under NSF-OPP awards 1543501, 1810976, 1542736, 1559691, 1043681, 1541332, 0753663, 1548562, and 1238993 and NASA award NNX10AN61G. Computer time provided through a Blue Waters Innovation Initiative. DEMs were produced using data from DigitalGlobe, Inc. Geospatial support for this work was provided by the Polar Geospatial Center under NSF-OPP awards 1043681 and 1559691. Any use of trade, firm, or product names is for descriptive purposes only and does not imply endorsement by the U.S. Government.

Barrand, N. E., Vaughan, D. G., Steiner, N., Tedesco, M., Kuipers Munneke, P., van den Broeke, M. R., & Hosking, J. S. (2013). Trends in Antarctic Peninsula surface melting conditions from observations and regional climate modeling. *Journal of Geophysical Research: Earth Surface*, *118*(1), 315–330. https://doi.org/10.1029/2012jf002559

Bell, R. E., Banwell, A. F., Trusel, L. D., & Kingslake, J. (2018). Antarctic surface hydrology and impacts on ice-sheet mass balance. *Nature Climate Change*, *8*(12), 1044–1052. https://doi.org/10.1038/s41558-018-0326-3

Bell, R. E., Chu, W., Kingslake, J., Das, I., Tedesco, M., Tinto, K. J., et al. (2017). Antarctic ice shelf potentially stabilized by export of meltwater in surface river. *Nature*, *544*(7650), 344–348. https://doi.org/10.1038/nature22048

Brangers, I., Lievens, H., Miège, C., Demuzere, M., Brucker, L., & De Lannoy, G. J. M. (2020). Sentinel-1 detects firn aquifers in the Greenland Ice Sheet. *Geophysical Research Letters*, *47*, e2019GL085192. https://doi.org/10.1029/2019GL085192

Braun, M., Humbert, A., & Moll, A. (2009). Changes of Wilkins Ice Shelf over the past 15 years and inferences on its stability. *The Cryosphere*, *3*(1), 41–56. https://doi.org/10.5194/tc-3-41-2009

Cherry, J., & Freeze, R. A. (1979). *Groundwater*. Englewood Cliffs, NJ: Prentice Hall.

Christianson, K., Kohler, J., Alley, R. B., Nuth, C., & van Pelt, W. J. J. (2015). Dynamic perennial firn aquifer on an Arctic glacier. *Geophysical Research Letters*, *42*, 1418–1426. https://doi.org/10.1002/2014GL062806

Conger, S. M., & McClung, D. M. (2009). Comparison of density cutters for snow profile observations. *Journal of Glaciology*, *55*(189), 163–169. https://doi.org/10.3189/002214309788609038

CReSIS. (2020). MCoRDS Data, Lawrence, Kansas, USA. Digital Media. http://data.cresis.ku.edu/. (n.d.).

Datta, R. T., Tedesco, M., Agosta, C., Fettweis, X., Kuipers Munneke, P., & van den Broeke, M. R. (2018). Melting over the northeast Antarctic Peninsula (1999–2009): Evaluation of a high-resolution regional climate model. *The Cryosphere*, *12*(9), 2901–2922. https://doi.org/10.5194/tc-12-2901-2018

Datta, R. T., Tedesco, M., Fettweis, X., Agosta, C., Lhermitte, S., Lenaerts, J. T. M., & Wever, N. (2019). The effect of foehn-induced surface melt on firn evolution over the northeast Antarctic peninsula. *Geophysical Research Letters*, *46*, 3822–3831. https://doi.org/10.1029/2018GL080845

Fornasini, P. (2008). *The uncertainty in physical measurements*. New York, NY: Springer New York. https://doi.org/10.1007/978-0-387-78650-6

Forster, R. R., Box, J. E., van den Broeke, M. R., Miège, C., Burgess, E. W., van Angelen, J. H., et al. (2014). Extensive liquid meltwater storage in firn within the Greenland Ice Sheet. *Nature Geoscience*, *7*(2), 95–98. https://doi.org/10.1038/ngeo2043

Fountain, A. G., & Walder, J. S. (1998). Water flow through temperate glaciers. *Reviews of Geophysics*, *36*(3), 299–328. https://doi.org/10.1029/97RG03579

Fricker, H. A., Bassis, J. N., Minster, B., & MacAyeal, D. R. (2005). ICESat's new perspective on ice shelf rifts: The vertical dimension. *Geophysical Research Letters*, *32*, L23S08. https://doi.org/10.1029/2005GL025070

Howat, I. M., Porter, C., Smith, B. E., Noh, M.-J., & Morin, P. (2019). The reference elevation model of Antarctica. *The Cryosphere*, *13*(2), 665–674. https://doi.org/10.5194/tc-13-665-2019

Humbert, A., & Braun, M. (2008). The Wilkins Ice Shelf, Antarctica: Break-up along failure zones. *Journal of Glaciology*, *54*(188), 943–944. https://doi.org/10.3189/002214308787780012

Humbert, A., Gross, D., Müller, R., Braun, M., van de Wal, R. S. W., van den Broeke, M. R., et al. (2010). Deformation and failure of the ice bridge on the Wilkins Ice Shelf, Antarctica. *Annals of Glaciology*, *51*(55), 49–55. https://doi.org/10.3189/172756410791392709

Jones, N. L. (1999). SEEP2D Primer. Environmental Modelling Research Laboratory, Brigham Young University.

Kingslake, J., Ely, J. C., Das, I., & Bell, R. E. (2017). Widespread movement of meltwater onto and across Antarctic ice shelves. *Nature*, *544*(7650), 349–352. https://doi.org/10.1038/nature22049

Koenig, L. S., Miège, C., Forster, R. R., & Brucker, L. (2014). Initial in situ measurements of perennial meltwater storage in the Greenland firn aquifer. *Geophysical Research Letters*, *41*, 81–85. https://doi.org/10.1002/2013GL058083

Kovacs, A., Gow, A. J., & Morey, R. M. (1995). The in-situ dielectric constant of polar firn revisited. *Cold Regions Science and Technology*, *23*(3), 245–256. https://doi.org/10.1016/0165-232X(94)00016-Q

Kuipers Munneke, P., Ligtenberg, S. R. M., van den Broeke, M. R., van Angelen, J. H., & Forster, R. R. (2014). Explaining the presence of perennial liquid water bodies in the firn of the Greenland Ice Sheet. *Geophysical Research Letters*, *41*, 476–483. https://doi.org/10.1002/2013GL058389

Lenaerts, J. T. M., Lhermitte, S., Drews, R., Ligtenberg, S. R. M., Berger, S., Helm, V., et al. (2017). Meltwater produced by wind-albedo interaction stored in an East Antarctic ice shelf. *Nature Climate Change*, *7*(1), 58–62. https://doi.org/10.1038/nclimate3180

Lenaerts, J. T. M., Medley, B., van den Broeke, M. R., & Wouters, B. (2019). Observing and modeling ice sheet surface mass balance. *Reviews of Geophysics*, *57*, 376–420. https://doi.org/10.1029/2018RG000622

Miège, C., Forster, R. R., Brucker, L., Koenig, L. S., Solomon, D. K., Paden, J. D., et al. (2016). Spatial extent and temporal variability of Greenland firn aquifers detected by ground and airborne radars. *Journal of Geophysical Research: Earth Surface*, *121*, 2381–2398. https://doi.org/10.1002/2016JF003869

Miller, O., Solomon, D. K., Miège, C., Koenig, L., Forster, R., Schmerr, N., et al. (2020). Hydrology of a perennial firn aquifer in southeast Greenland: An overview driven by field data. *Water Resources Research*, *56*, e2019WR026348. https://doi.org/10.1029/2019WR026348

Miller, O., Solomon, D. K., Miège, C., Koenig, L., Forster, R., Schmerr, N., et al. (2018). Direct evidence of meltwater flow within a firn aquifer in Southeast Greenland. *Geophysical Research Letters*, *45*, 207–215. https://doi.org/10.1002/2017GL075707

Miller, O. L., Solomon, D. K., Miège, C., Koenig, L. S., Forster, R. R., Montgomery, L. N., et al. (2017). Hydraulic conductivity of a firn aquifer in Southeast Greenland. *Frontiers in Earth Science*, *5*, 38. https://doi.org/10.3389/feart.2017.00038

Montgomery, L., Koenig, L., Lenaerts, J. T. M., & Kuipers Munneke, P. (2020). Accumulation rates (2009–2017) in Southeast Greenland derived from airborne snow radar and comparison with regional climate models. *Annals of Glaciology*, *61*(81), 225–233. https://doi.org/10.1017/aog.2020.8

Montgomery, L. N., Schmerr, N., Burdick, S., Forster, R. R., Koenig, L., Legchenko, A., et al. (2017). Investigation of firn aquifer structure in southeastern Greenland using active source seismology. *Frontiers in Earth Science*, *5*, 10. https://doi.org/10.3389/feart.2017.00010

Noël, B., van de Berg, W. J., van Wessem, J. M., van Meijgaard, E., van As, D., Lenaerts, J. T. M., et al. (2018). Modelling the climate and surface mass balance of polar ice sheets using RACMO2—Part 1: Greenland (1958–2016). *The Cryosphere*, *12*(3), 811–831. https://doi.org/10.5194/tc-12-811-2018

Phillips, H. A. (1998). Surface meltstreams on the Amery Ice Shelf, East Antarctica. *Annals of Glaciology*, *27*, 177–181. https://doi.org/10.3189/1998AoG27-1-177-181

Pitrak, M., Mares, S., & Kobr, M. (2007). A simple borehole dilution technique in measuring horizontal ground water flow. *Ground Water*, *45*(1), 89–92. https://doi.org/10.1111/j.1745-6584.2006.00258.x

Poinar, K., Joughin, I., Lilien, D., Brucker, L., Kehrl, L., & Nowicki, S. (2017). Drainage of Southeast Greenland firn aquifer water through crevasses to the bed. *Frontiers in Earth Science*, *5*, 5. https://doi.org/10.3389/feart.2017.00005

Pollard, D., DeConto, R. M., & Alley, R. B. (2015). Potential Antarctic Ice Sheet retreat driven by hydrofracturing and ice cliff failure. *Earth and Planetary Science Letters*, *412*, 112–121. https://doi.org/10.1016/j.epsl.2014.12.035

Pritchard, H. D., Ligtenberg, S. R. M., Fricker, H. A., Vaughan, D. G., van den Broeke, M. R., & Padman, L. (2012). Antarctic ice-sheet loss driven by basal melting of ice shelves. *Nature*, *484*(7395), 502–505. https://doi.org/10.1038/nature10968

Rignot, E., Jacobs, S., Mouginot, J., & Scheuchl, B. (2013). Ice-shelf melting around Antarctica. *Science*, *341*(6143), 266–270. https://doi.org/10.1126/science.1235798

Scambos, T. A. (2004). Glacier acceleration and thinning after ice shelf collapse in the Larsen B embayment, Antarctica. *Geophysical Research Letters*, *31*, L18402. https://doi.org/10.1029/2004GL020670

Scambos, T. A., Fricker, H., Liu, C.-C., Bohlander, J., Fastook, J., Sargent, A., et al. (2009). Ice shelf disintegration by plate bending and hydro-fracture: Satellite observations and model results of the 2008 Wilkins Ice Shelf break-ups. *Earth and Planetary Science Letters*, *280*(1–4), 51–60. https://doi.org/10.1016/j.epsl.2008.12.027

Scambos, T. A., Hulbe, C., Fahnestock, M., & Bohlander, J. (2000). The link between climate warming and break-up of ice shelves in the Antarctic Peninsula. *Journal of Glaciology*, *46*(154), 516–530. https://doi.org/10.3189/172756500781833043

Scambos, T., Hulbe, C., & Fahnestock, M. (2003). Climate-induced ice shelf disintegration in the Antarctic Peninsula. In E. Domack, A. Levente, A. Burnet, R. Bindschadler, P. Convey, & M. Kirby (Eds.), *Antarctic Research Series* (pp. 79–92). Washington, D. C: American Geophysical Union. https://doi.org/10.1029/AR079p0079

Siegert, M., Atkinson, A., Banwell, A., Brandon, M., Convey, P., Davies, B., et al. (2019). The Antarctic Peninsula under a 1.5°C global warming scenario. *Frontiers in Environmental Science*, *7*, 102. https://doi.org/10.3389/fenvs.2019.00102

Smith, B., Fricker, H. A., Gardner, A. S., Medley, B., Nilsson, J., Paolo, F. S., et al. (2020). Pervasive ice sheet mass loss reflects competing ocean and atmosphere processes. *Science*, *368*(6496), 1239–1242. https://doi.org/10.1126/science.aaz5845

Studinger, M. (2014, updated 2020). IceBridge ATM L2 Icessn Elevation, Slope, and Roughness, Version 2. [Subset Used: 2014]. Boulder, Colorado USA. NASA National Snow and Ice Data Center Distributed Active Archive Center. https://doi.org/10.5067/CPRXXK3F39RV. [Date Accessed: 2018].

Vaughan, D. G., Mantripp, D. R., Sievers, J., & Doake, C. S. M. (1993). A synthesis of remote sensing data on Wilkins Ice Shelf, Antarctica. *Annals of Glaciology*, *17*, 211–218. https://doi.org/10.3189/S0260305500012866

van Wessem, J. M., Ligtenberg, S. R. M., Reijmer, C. H., van de Berg, W. J., van den Broeke, M. R., Barrand, N. E., et al. (2016). The modelled surface mass balance of the Antarctic peninsula at 5.5 km horizontal resolution. *The Cryosphere*, *10*(1), 271–285. https://doi.org/10.5194/tc-10-271-2016

van Wessem, J. M., Steger, C. R., Wever, N., & van den Broeke, M. R. (2020). *Modelling perennial firn aquifers in the Antarctic Peninsula (1979–2016)* (preprint). Snow/Snow Physics. https://doi.org/10.5194/tc-2020-148